ADVANCED ENERGY MATERIALS
www.advenergymat.de

MXene-Contacted Silicon Solar Cells with 11.5% Efficiency

Hui-Chun Fu, Vinoth Ramalingam, Hyunho Kim, Chun-Ho Lin, Xiaosheng Fang, Husam N. Alshareef,* and Jr-Hau He**

MXene, a new class of 2D materials, has gained significant attention owing to its attractive electrical conductivity, tunable work function, and metallic nature for wide range of applications. Herein, delaminated few layered $Ti_3C_2T_x$ MXene contacted Si solar cells with a maximum power conversion efficiency (PCE) of ≈11.5% under AM1.5G illumination are demonstrated. The formation of an Ohmic junction of the metallic MXene to n^+-Si surface efficiently extracts the photogenerated electrons from n^+np^+-Si, decreases the contact resistance, and suppresses the charge carrier recombination, giving rise to excellent open-circuit voltage and short-circuit current density. The rapid thermal annealing process further improves the electrical contact between $Ti_3C_2T_x$ MXene and n^+-Si surface by reducing sheet resistance, increasing electrical conductivity, and decreasing cell series resistance, thus leading to a remarkable improvement in fill factor and overall PCE. The work demonstrated here can be extended to other MXene compositions as potential electrodes for developing highly performing solar cells.

2D nanomaterials have been identified as promising materials for future electronics and optoelectronic based devices including solar cells, light-emitting diodes, transistors, memory devices, photodetectors, laser applications, etc.[1–8] In particular, 2D material-based solar cells have gained significant attention because of their easy device fabrication process, excellent optical properties, solution processable approach, low temperature fabrication, and tunable band structure at nanoscale dimensions.[9–12] For example, 2D graphene with multiple optoelectronic properties such as excellent electrical conductivity and better optical transmittance can be an ideal candidate to combine with Si solar cells. Li et al. fabricated the first graphene on n-Si Schottky junction based solar cell by simply transferring graphene onto an n-Si wafer.[13] The Schottky junction formed at the graphene/n-Si interface enhances the power conversion efficiency (PCE) up to 1.5%. Graphene has also been utilized as a transparent electrode in graphene/Si heterojunction solar cells with a maximum PCE of 4.98%.[14] In order to further improve the performance of graphene based solar cells, a series of chemical modifications which include chemical doping, molecular doping, ion doping, nanoparticle decoration, covalent, and noncovalent functionalization on graphene have been demonstrated.[15–18] Other than graphene, 2D transition metal dichalcogenides (TMDs) have also been successfully integrated with Si solar cells.[2] For example, chemical vapor deposition (CVD) fabricated monolayer MoS_2/p-Si heterojunction was achieved with a maximum PCE of 5.23%.[2] The monolayer MoS_2 with p-Si forms a type-II heterojunction, which facilitates the charge carrier separation and thereby improves the PCE of MoS_2/p-Si device. Moreover, an atomic 2D monolayer WSe_2–MoS_2 p–n lateral heterojunction solar cell has shown a PCE up to 2.56%.[19] However, when fabricating large area TMDs and graphene, there are complex steps involved in the fabrication process, which present major challenges that greatly hamper the development of 2D material-based solar cells. Therefore, it is of great importance to identify a new family of 2D materials with the desired electronic properties. Easily processable and scalable approaches would be an alternative to overcome the limitations associated with the existing 2D material-based solar cells.

MXene is a new class of 2D materials made up of either transition metal carbides/nitrides or carbo nitrides.[20,21] MXene is generally represented as $M_{n+1}X_nT_x$, where M is an early transition metal (Ti, Mo, Nb, or V), X is carbide (C) or nitride (N), and T_x represents the surface terminated functional groups (F, OH, and O).[22] These 2D MXene sheets can be synthesized by selectively etching the main group element (A) from the ternary transition metal carbides/or nitrides called MAX (M: transition metals, A: main group element, X: C/or N) phase using different etchants such as hydrofluoric (HF) or lithium fluoride/hydrochloric acid (LiF/HCl) mixtures.[23,24] MXene possesses many attractive properties that include excellent electronic conductivity, catalytically active basal planes with exposed metal sites, and hydrophilic surface functionalities

Dr. H.-C. Fu, Dr. V. Ramalingam, Dr. C.-H. Lin, Prof. J.-H. He
Computer, Electrical, and Mathematical Sciences and Engineering
King Abdullah University of Science and Technology
Thuwal 23955–6900, Kingdom of Saudi Arabia
E-mail: jrhau.he@kaust.edu.sa

H. Kim, Prof. H. N. Alshareef
Materials Science and Engineering
Physical Science and Engineering Division
King Abdullah University of Science and Technology (KAUST)
Thuwal 23955–6900, Kingdom of Saudi Arabia
E-mail: husam.alshareef@kaust.edu.sa

Prof. X. Fang
Department of Materials Science
Fudan University
Shanghai 200433, P. R. China
E-mail: xshfang@fudan.edu.cn

The ORCID identification number(s) for the author(s) of this article can be found under https://doi.org/10.1002/aenm.201900180.

DOI: 10.1002/aenm.201900180

(—O and—OH groups) to form easy interactions with water molecules, semiconductors, and unique structures.[20] These interesting properties turn MXene into a promising candidate for several energy conversion and storage applications including supercapacitors, batteries, hydrogen evolution reaction (HER), oxygen evolution reaction (OER), photocatalytic hydrogen production, dye degradation, etc.[20,21,23,25–30] For example, Ti_3C_2 MXene served as an efficient cocatalyst along with CdS photocatalyst and achieved an excellent visible light photocatalytic hydrogen production performance.[20] On the other hand, with very high volumetric capacitance and ultrafast cycling properties, titanium carbide ($Ti_3C_2T_x$) MXene has made tremendous progress in the field of supercapacitors and batteries.[21,31] For instance, Gogotsi and co-workers fabricated the $Ti_3C_2T_x$ MXene hydrogels for supercapacitor application.[32] The $Ti_3C_2T_x$ MXene hydrogels possess a high volumetric capacitance of 1500 F cm^3. This value is quite comparable with the commercial supercapacitor electrodes using RuO_2. Likewise, highly transparent and conductive Ti_3C_2 MXene have been demonstrated as a potential electrode for solid state supercapacitor.[33] Besides, layered structure with uniform interlayer spacing of 2D MXene can allow the intercalation of Na, Li, and K ions for electrochemical energy storage applications.[30] MXene thin film have also been used as a flexible transparent conducting film.[30] The Ti_3C_2 MXene film with a thickness of ≈5 nm exhibits an outstanding optical transmittance of ≈90%.[34] However, MXene in the field of optoelectronics has seldom been investigated. Kang et al. has studied the $Ti_3C_2T_x$ MXene–silicon van der Walls heterostructure for ultrafast vertical junction photodetector applications.[35] The $Ti_3C_2T_x$ MXene forms the Schottky junction at the $Ti_3C_2T_x$ MXene/n-Si interface. Moreover, $Ti_3C_2T_x$ MXene applied to $Ti_3C_2T_x$ MXene/n-Si not only serves as a transparent electrode but also improves the photogenerated charge carrier separation and transportation. Recently, $Ti_3C_2T_x$ MXene as a metal contact has performed well in thin film transistor (TFTs) applications.[36]

Inspired by MXene electrical properties, herein we have fabricated $Ti_3C_2T_x$ MXene contacted Si solar cells. 2D $Ti_3C_2T_x$ MXene is significantly more conducting than solution derived graphene,[37] so it could in principle be a better contact material for solar cells. Thus, the delaminated few layered $Ti_3C_2T_x$ was drop casted on heavily doped n^+ surface of n^+np^+-Si solar cell, achieving impressive fill factor (FF), short-circuit current density (J_{sc}), and open-circuit voltage (V_{oc}) by minimizing contact resistance and recombination by repelling the minority carriers away from the high-combination contact region. Rapid thermal annealing (RTA) improves the electrical contact between $Ti_3C_2T_x$ MXene and Si, not only reducing the sheet resistance of $Ti_3C_2T_x$ MXene films but also improving the cell series resistance (R_s), and enhancing the PCE up to ≈11.5% with 20% improvement in the FF, which is exceptional. In addition to impressive solar performance of MXene contacted Si cells, our results also address the physics governing electrical contact across the MXene and Si interface, which is critical to further improvement for similar MXene contacted devices.

A schematic illustration for the synthesis of 2D $Ti_3C_2T_x$ MXene nanosheets and $Ti_3C_2T_x$ MXene contacted Si solar cell device fabrication is shown in **Figure 1**a. The $Ti_3C_2T_x$ MXene was synthesized from Ti_3AlC_2 MAX phase using LiF and HCl solution mixture, which can selectively remove the Al layers from the MAX phase and thereby produce multilayer $Ti_3C_2T_x$ MXene.[36] Next, the delaminated few layered $Ti_3C_2T_x$ MXene sheets were collected via a mild hand shaking process followed by several centrifugation cycles and repeated washing. Figure 1b shows the schematic of $Ti_3C_2T_x$ MXene contacted Si solar cells. The light-harvesting (np^+-Si) side is achieved by 70 nm phosphorus diffusion and form textured micropyramidal surface (as shown in Figure 1c), while the MXene/Si (nn^+-Si) side is formed by 400 nm boron alloying at the opposite surfaces (textured microgroove structures as depicted in Figure 1d) to form a sandwich structure onto the n-type Si, which promotes internal light reflection and light absorption in the bulk of the cell. The photogenerated electrons and holes migrate toward the $Ti_3C_2T_x$ MXene (nn^+-Si) and Ag/Al finger-patterned metal grids (np^+-Si) sides of the devices, respectively, due to the cascade energy band structure. The intentional n^+np^+ structure provides several advantages such as i) lowering the pronounced Schottky contact resistance at the $Ti_3C_2T_x$ MXene/Si interface, ii) minimizing the impact of surface recombination on the photovoltage and photocurrent, and iii) reducing the recombination of the photogenerated carriers between $Ti_3C_2T_x$ MXene/Si interfaces by introducing a barrier to holes at the n^+n interface. Most importantly, thermal diffusion was applied to form a very thin n^+-Si surface as the back surface field prior to $Ti_3C_2T_x$ MXene deposition to minimize contact resistance and recombination between $Ti_3C_2T_x$ MXene and Si by keeping minority carriers (in this study, holes) away from high recombination $Ti_3C_2T_x$ MXene/n^+-Si contact. Afterward, a 10 nm Al_2O_3 was coated to p^+-Si surface, ensuring wide-range omnidirectional light-absorption and suppressing carrier recombination by the surface defect. Additionally, wide-range omnidirectional light-absorption can be achieved by introducing a pinhole-free antireflection coating (ARC) of SiN_x (60 nm) which were deposited conformally on the pyramids of the light harvesting side using atomic layer deposition. SiN_x is used because of its stability with high-temperature contact firing for the Si solar cell, and its annealing induced capability for hydrogen passivation of the boundaries and defects.[38] Next, 300 nm thick Ag/Al finger-patterned metal grids were deposited by screen-printing on the light-harvesting side on which Ag/Al metal electrodes create an Ohmic contact with p^+-Si and thereby extract the photogenerated holes; meanwhile, Ag/Al metal electrodes result in excellent light harvesting ability with minor shadowing effect. Afterward, we drop casted $Ti_3C_2T_x$ MXene on n^+-Si surface which acted as a metal electrode to extract the photogenerated electrons from Si. The detailed device fabrication is shown in the Experimental Section. As shown in Figure 1e, drop-casted $Ti_3C_2T_x$ MXene is uniformly covered on the n^+-Si microgroove surface. Drop casting is an effective method that does not require hydrophilic substrates.[35] Furthermore, the $Ti_3C_2T_x$ MXene contacted Si device was RTA processed under inert atmosphere. The RTA process can improve electrical contact between $Ti_3C_2T_x$ MXene and n^+np^+-Si, thus leading to enhanced charge carrier transportation and decreased contact resistance. Balci and Kocabas have done the systematic investigation on graphene–metal contacts device before and after rapid thermal annealing process.[39] The device after rapid thermal annealing process reduced the contact resistance on graphene–metal junction, thus to achieve reproducible device performance.

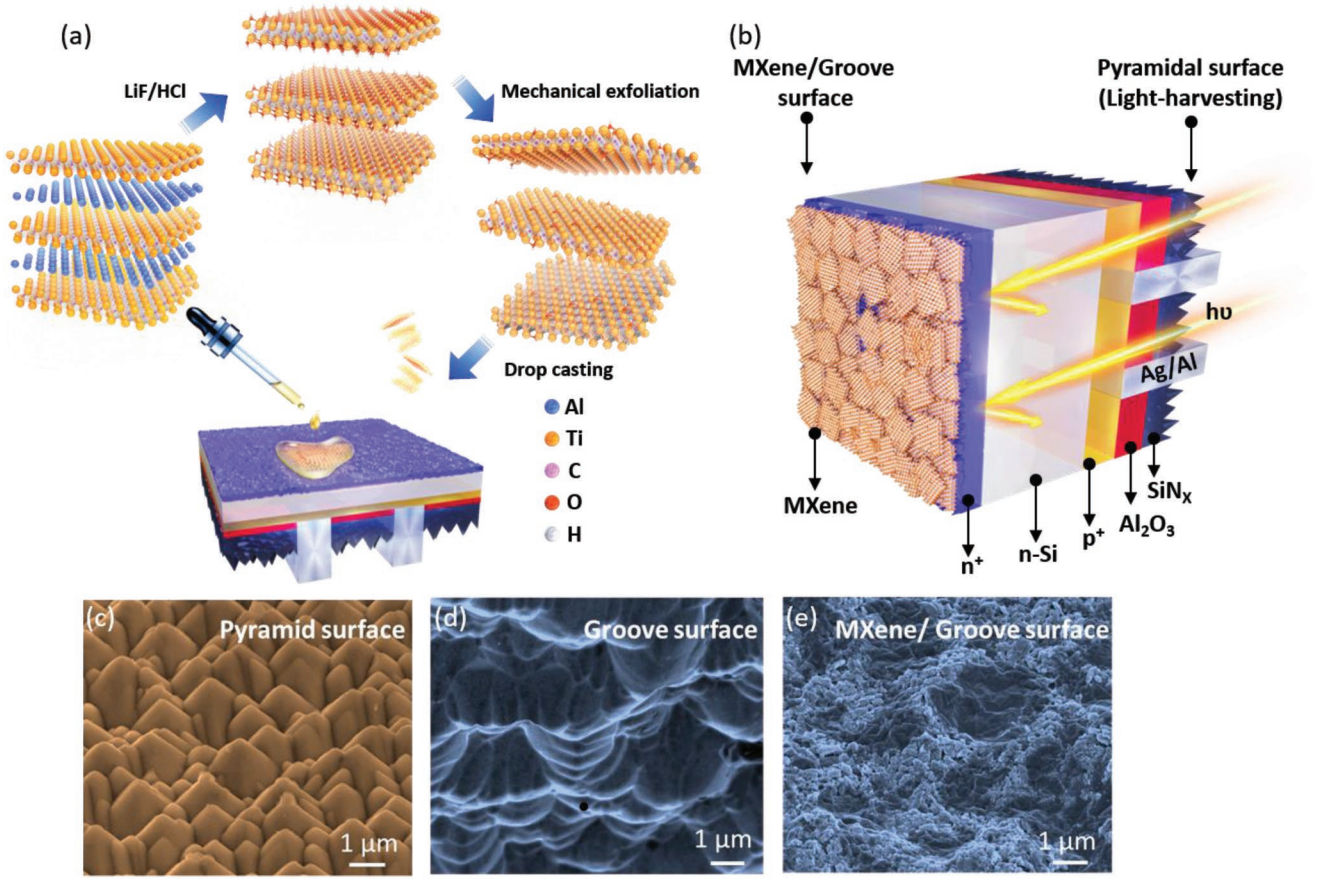

Figure 1. a) Schematic representation for the synthesis of delaminated $Ti_3C_2T_x$ MXene sheets and the fabrication of $Ti_3C_2T_x$ MXene/n^+np^+-Si solar cell device by drop casting delaminated $Ti_3C_2T_x$ MXene on n^+-Si surface. b) device architecture of $Ti_3C_2T_x$ MXene/n^+np^+-Si solar cell. c–e) FE-SEM image of n^+ side (light illumination side), p^+ side, and $Ti_3C_2T_x$ MXene deposited n^+side of n^+np^+-Si solar cell.

Figure 2a shows the typical X-ray diffraction (XRD) patterns of Ti_3AlC_2 MAX powder and delaminated $Ti_3C_2T_x$ MXene sheets. The XRD peak at $2\theta = 9.5°$ corresponds to the (002) planes of the Ti_3AlC_2 MAX phase, which is consistent with previously reported literature.[24,36] The XRD patterns of $Ti_3C_2T_x$ MXene show a peak shift to lower angles ($2\theta = 6.8°$) compared to that of Ti_3AlC_2 MAX, indicating the successful exfoliation of few layered $Ti_3C_2T_x$ MXene and the existence of surface terminated functionalities and water molecules between the MXene layers.[22,40] The Raman spectra of Ti_3AlC_2 MAX and $Ti_3C_2T_x$ MXene phases are displayed in Figure 2b. The Ti_3AlC_2 MAX phase exhibits distinct sharp Raman peaks, which agree well with the theoretically predicted wavenumbers (Table S1, Supporting Information).[41] Two minor peaks at 395 and 585 cm^{-1} can be attributed to possible impurity or defects in the commercially purchased Ti_3AlC_2 powder. The $Ti_3C_2T_x$ MXene has broader Raman peaks which are probably due to the coexistence of various surface terminated functional groups that can have this effect on phonon dispersion of $Ti_3C_2T_x$ MXene.[36] Moreover, absence of peak at 144 cm^{-1} reveals that no titanium dioxide has been formed on the surface of $Ti_3C_2T_x$ MXene. In order to study the effect of RTA on $Ti_3C_2T_x$ MXene, Raman spectra was obtained for the drop-casted $Ti_3C_2T_x$ MXene films before and after RTA process at different temperature (Figure S1, Supporting Information). It is seen that $Ti_3C_2T_x$ MXene's crystal structure and Raman modes remain the same for the samples before and after RTA treatment under Ar atmosphere. No additional peaks were found after RTA process for all temperatures. This evidences that no unwanted changes occurred during RTA process. We believe that $Ti_3C_2T_x$ MXene films are not subject to oxidation or decomposition as long as the ambient is well controlled without oxygen and water. In addition, it has been reported that the $Ti_3C_2T_x$ MXene was stable during thermal annealing up to 800 °C under inert atmosphere.[42–44] Furthermore, X-ray photoelectron spectroscopy (XPS) analysis was performed to confirm the successful preparation of $Ti_3C_2T_x$ MXene. As shown in Figure 2c, high resolution Ti2p XPS spectra depicts $Ti2p_{3/2}$ and $Ti2p_{1/2}$ peaks at 455.2 and 461.2 eV, which indicates the bonding between Ti and C in $Ti_3C_2T_x$ MXene, respectively.[45] Likewise, high resolution C1s XPS spectra shows that an obviously intense peak at 281.7 eV is related to Ti—C bond while a small peak at 284.8 eV is assigned to C—C bond (Figure 2d).[46] Field emission scanning electron microscope (FE-SEM) image and atomic force microscopy (AFM) image of $Ti_3C_2T_x$ MXene shows the presence of a delaminated few layered $Ti_3C_2T_x$ MXene with well-defined 2D nanosheet morphology (Figure 2e,f). Besides, cross sectional FE-SEM image shows that the few-layered $Ti_3C_2T_x$

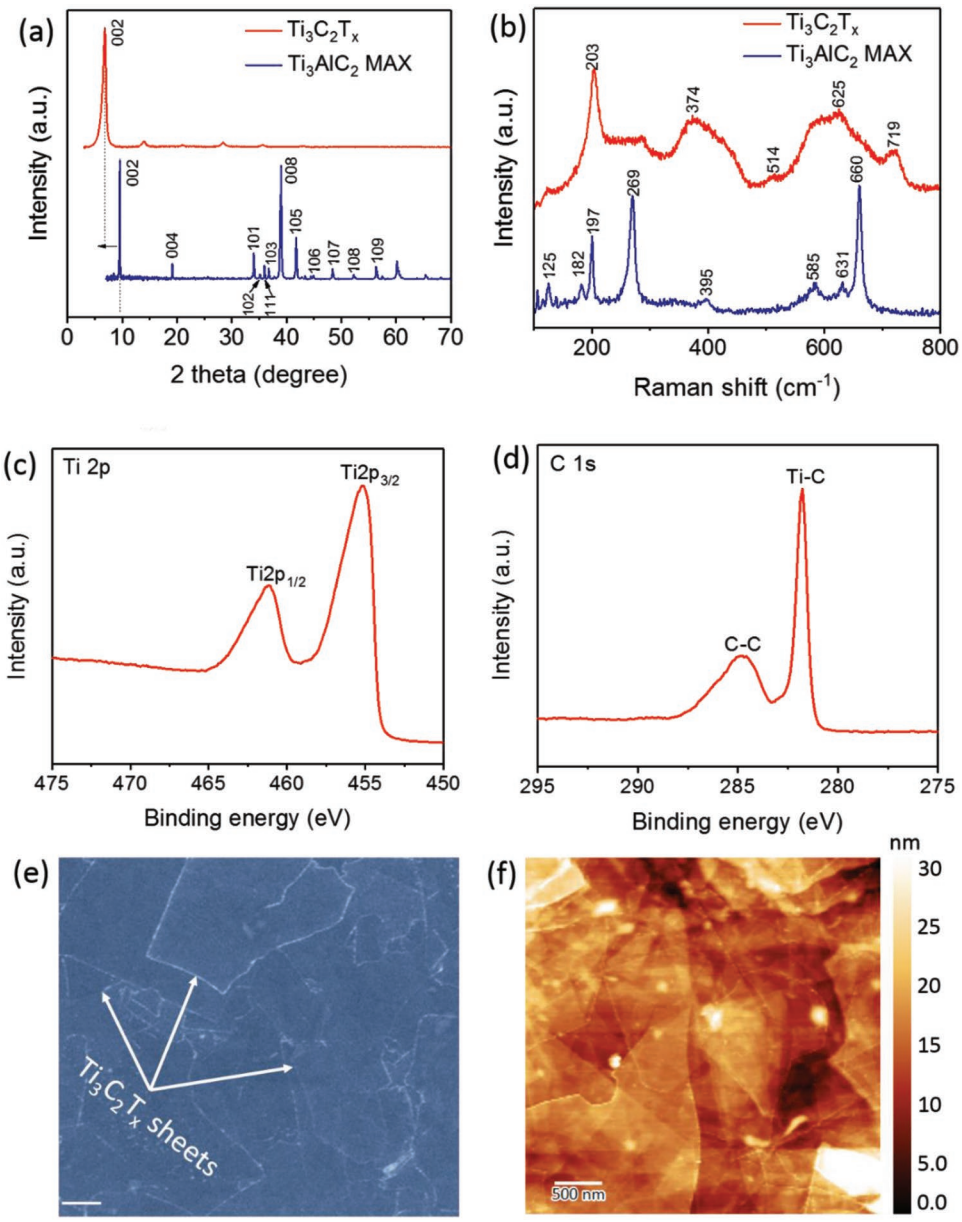

Figure 2. a) X-ray diffraction (XRD) patterns of Ti_3AlC_2 MAX and delaminated $Ti_3C_2T_x$ MXene sheets. b) Raman spectra of Ti_3AlC_2 MAX and $Ti_3C_2T_x$ MXene. c,d) High resolution Ti2p and C1s X-ray photoelectron spectroscopy (XPS) spectra of $Ti_3C_2T_x$ MXene. e) Field emission scanning electron microscopy (FE-SEM) image of $Ti_3C_2T_x$ MXene. f) Atomic force microscopy (AFM) image of $Ti_3C_2T_x$ MXene.

MXene sheets are uniformly covered by the microgroove Si surface of n^+pp^+-Si solar cell (Figure S2, Supporting Information).

In order to gain insight into the electronic structures of the MXene/n^+np^+-Si solar cells, the work function of $Ti_3C_2T_x$ MXene was calculated using scanning Kelvin probe microscopy (SKPM). **Figure 3**a shows the AFM image and SKPM mapping area of drop-casted $Ti_3C_2T_x$ MXene. The topography and surface potential of n^+-Si and $Ti_3C_2T_x$ MXene were measured along the area marked by the red square shown in Figure 3a. The topography and surface potential are represented by red and blue curves in Figure 3b. The thickness of drop-casted $Ti_3C_2T_x$ MXene nanosheets from n^+-Si substrate is measured to be ≈12 nm, suggesting the existence of few layered $Ti_3C_2T_x$ MXene during the measurement. The work functions of $Ti_3C_2T_x$ MXene (Φ_{MXene}) and n^+-Si ($\Phi_{n+\text{-}Si}$) were estimated based on the surface potential difference between $Ti_3C_2T_x$ MXene and n^+-Si using the SKPM method.[47,48] The surface potential difference of 0.18 V between n^+-Si and $Ti_3C_2T_x$ MXene was obtained. Therefore, the work functions of n^+-Si and $Ti_3C_2T_x$ MXene were estimated to be 4.10 and 4.28 eV, respectively (**Table 1**). The work functions of the most widely used metal electrodes are summarized in **Table 2**. Based on the calculated work functions, we proposed the band diagram of the $Ti_3C_2T_x$ MXene/n^+np^+-Si solar cell as illustrated in Figure 3c. The work function of $Ti_3C_2T_x$ MXene is ≈0.18 eV higher than n^+-Si, which is sufficient to form an Ohmic contact at $Ti_3C_2T_x$ MXene/n^+-Si

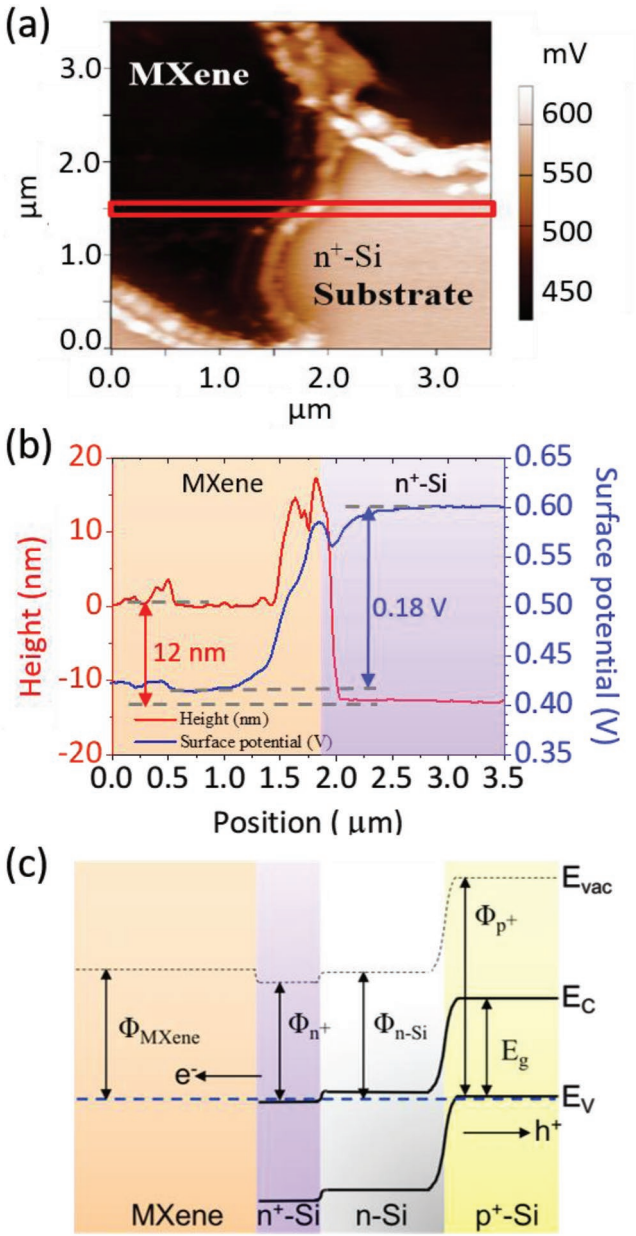

Figure 3. a) AFM topography image/scanning kelvin probe mapping (marked area) on $Ti_3C_2T_x$ MXene/n^+-Si. b) Topography and surface potential of $Ti_3C_2T_x$ MXene/n^+-Si. c) Proposed band diagram of $Ti_3C_2T_x$ MXene/n^+np^+-Si solar cell based on the calculated work function measurements. Φ is a work function, E_g is energy bandgap of Si, and E_c and E_v are the conduction band and valence band.

interface. High recombination rates at the surface are known to have a particularly detrimental impact on the devices.[49,50] The work functions of $Ti_3C_2T_x$ MXene films after RTA treatment at 100, 200, 300, and 400 °C are estimated to be 4.31, 4.29, 4.28, and 4.28 eV, respectively (Figure S3, Supporting Information). These work function values are quite close to the work function of $Ti_3C_2T_x$ MXene (4.28 eV) before RTA treatment (Figure 3b). A small change in the work function value observed for RTA processed $Ti_3C_2T_x$ MXene might be due to the removal of oxygen rich surface functional groups during RTA treatment under Ar atmosphere. Herein, the $Ti_3C_2T_x$ MXene in contact with n^+-Si back surface field (consisting of a higher doped surface) is expected to have a major impact both on the J_{SC} and the V_{OC} by forming the superior Ohmic contact and introducing a barrier to minority carrier flow to the surface near $Ti_3C_2T_x$ MXene, resulting in photoexcited electrons transferred from n^+-Si to $Ti_3C_2T_x$ MXene electrode whereas the photogenerated holes transfer to Ag finger electrode at p^+-Si side. The interaction between $Ti_3C_2T_x$ MXene and Si surface was studied using contact angle measurement. The contact angle between the $Ti_3C_2T_x$ MXene solution and n^+-Si is shown in Figure S4 in the Supporting Information. The contact angle as small as 37.6° indicates that the surface tension is not very strong and the shrinking during the drop casting is moderate. In our solar cell design, $Ti_3C_2T_x$ MXene film was coated on the microgroove structured surface and it is difficult to study the homogeneity property since the 2D $Ti_3C_2T_x$ MXene films are too thin compared to the microgroove structures. Instead, the $Ti_3C_2T_x$ MXene was drop casted on a flat n^+-Si substrate to study the homogeneity property of drop casted $Ti_3C_2T_x$ MXene film. The surface morphology at three different edges of $Ti_3C_2T_x$ MXene films was studied using a Zygo profilometer (Figure S5, Supporting Information). The root-mean-square roughness of $Ti_3C_2T_x$ MXene films at three different edges was estimated to be 97, 82, and 87 nm, respectively. Therefore, although the surface tension makes moderate shrinking and influences on the homogeneity of $Ti_3C_2T_x$ MXene film, it is still controllable and acceptable. Moreover, photograph image shown in Figure S6 in the Supporting Information confirms the uniform coverage of $Ti_3C_2T_x$ MXene film on glass substrate using drop-casting process. In addition, we performed a simple experiment using Kapton tape to study the adhesion between $Ti_3C_2T_x$ MXene and n^+np^+-Si cell before and after RTA treatment. As depicted in Figure S7b in the Supporting Information photograph image, $Ti_3C_2T_x$ MXene on n^+np^+-Si cell before RTA is unstable and it peel-off easily when removing the Kapton tape. Interestingly, $Ti_3C_2T_x$ MXene film annealed at 300 °C looks relatively stable and only the part of portions at the edge gets peel-off slightly, indicates the better adhesion between $Ti_3C_2T_x$ MXene and Si cell during RTA (Figure S7c, Supporting Information). Furthermore, we have performed the same experiment with $Ti_3C_2T_x$ MXene drop casted on glass substrate (Figure S8, Supporting Information). As expected, the drop-casted $Ti_3C_2T_x$ MXene film on glass substrates after RTA treatment at 300 °C is quite stable compared to that of the $Ti_3C_2T_x$ MXene/glass before RTA (Figure S8b–d, Supporting Information). These experiments clearly demonstrate that the RTA process plays a significant

Table 1. Work function of $Ti_3C_2T_x$ MXene/n^+np^+-Si solar cell (eV).

Φ_{MXene}	Φ_{n+-Si}	Φ_{n-Si}	Φ_{p+-Si}
4.28	4.10	4.30	5.25

Table 2. Work function of metal electrodes (eV).

Φ_{Ti}	Φ_{Au}	Φ_{Ag}	Φ_{Al}
4.33	5.10–5.47	4.26–4.74	4.06–4.26

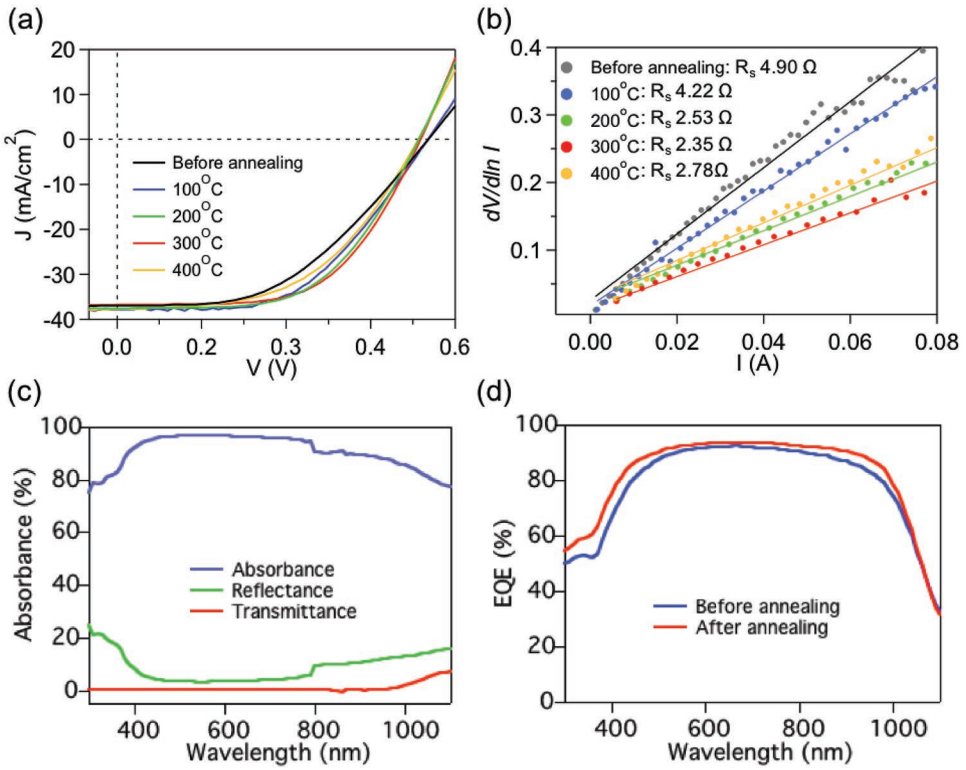

Figure 4. a) Current density–voltage (*J*–*V*) characteristics of $Ti_3C_2T_x$ MXene/n^+np^+-Si solar cell before and after rapid thermal annealing (RTA) process from 100–400 °C upon AM 1.5 illumination (measured in air atmosphere at a scan rate of 20 mV s^{-1}). b) The series resistance (R_s) values extrapolated from d*V*/dln *I* versus *I* curves before and after RTA process. c) Absorbance, reflection, and transmittance spectra of n^+np^+-Si solar cell. d) External quantum efficiency (EQE) spectra of $Ti_3C_2T_x$ MXene/n^+np^+-Si solar cells before and after RTA treatment at 300 °C.

role to improve the adhesion between $Ti_3C_2T_x$ MXene and Si surface, which further leads to the enhancement in the PCE of the device.

Figure 4a shows the current density–voltage (*J*–*V*) characteristics of the $Ti_3C_2T_x$ MXene/n^+np^+-Si solar cells upon AM1.5G illumination before and after RTA at different temperatures (100, 200, 300, and 400 °C) under Ar atmosphere and their corresponding photovoltaic parameters are summarized in **Table 3**. The $Ti_3C_2T_x$ MXene/n^+np^+-Si solar cell before RTA shows PCE of 9.53% with J_{sc} = 36.89 mA cm^{-2}, V_{oc} = 0.55 V, and FF = 46.79%. The performance of the device improved gradually with respect to RTA temperature up to 300 °C and then worsened when the temperature increased to 400 °C. The device annealed at 300 °C shows the highest PCE of ≈11.5% with J_{sc} = 36.70 mA cm^{-2}, V_{oc} = 0.54 V, and FF = 57.99%. It can be clearly seen that the 300 °C annealing gives rise to the 20% enhancement in FF, thus leading to improved PCE. Moreover, it was found from the following literature that the RTA process under inert atmosphere can increase the FF of solar cell compared to that of device without RTA process.[51,52] These literature reports reveal that the RTA treatment can improve the FF of the solar cell device as we have also noted the similar trend in the present work. In order to understand the effect of RTA on the $Ti_3C_2T_x$ MXene contact to Si, we measured the electrical properties of $Ti_3C_2T_x$ MXene films before and after RTA using Hall measurements. The corresponding results are summarized in Table S2 in Supporting Information. The conductivity of $Ti_3C_2T_x$ MXene films before and after 100, 200, 300, and 400 °C annealing was estimated to be 2.113×10^3, 2.277×10^3, 2.425×10^3, 2.518×10^3, and 0.975×10^3 Ω^{-1} cm^{-1}, respectively. The conductivity of the $Ti_3C_2T_x$ MXene film increased with RTA temperature up to 300 °C. It can be observed that the conductivity of $Ti_3C_2T_x$ MXene film annealed at 400 °C decreased rapidly, indicating that the $Ti_3C_2T_x$ MXene film is not stable at the higher temperatures and it tends to degrade slowly. Furthermore, cell series resistance (R_s) for the $Ti_3C_2T_x$ MXene contacted Si solar cell device before and after RTA was calculated by extracting the slope value from the plots of d*V*/dln *I* versus *I* (Figure 4b). The device before and after RTA at 100, 200, 300, and 400 °C offers R_s values of 4.90, 4.22, 2.53, 2.38, and 2.78 Ω, respectively, in which a 300 °C annealed device exhibits low R_s. The R_s of a solar cell originates mostly from the contact between the metal contact and Si, and the resistance of the Si

Table 3. The photovoltaic parameters of $Ti_3C_2T_x$ MXene/n^+np^+-Si solar cell devices before and after RTA process.

[°C]	V_{oc} [V]	J_{sc} [mA cm^{-2}]	FF [%]	PCE [%]
Before RTA	0.55	36.89	46.79	9.53
100	0.55	38.09	50.21	10.52
200	0.54	37.58	56.05	11.28
300	0.54	36.70	57.99	11.47
400	0.53	37.76	50.79	10.26

and contact metal. The high R_s will reduce the short-circuit current without affecting the open-circuit voltage. Accordingly, the FF can be partially improved by the low sheet resistance of $Ti_3C_2T_x$ MXene films. The observed changes in electrical conductivity and R_s with respect to RTA temperature are consistent with the changes in solar performance. Therefore, the enhancement after RTA can be attributed to the improvement in electrical contact formation between the metallic $Ti_3C_2T_x$ MXene and Si, increased conductivity, low R_s, and associated reduction of Ohmic losses, significantly boosting the overall PCE of $Ti_3C_2T_x$ MXene contacted Si solar cell. Additionally, the heavily doped n^+-Si can create an Ohmic contact with metallic $Ti_3C_2T_x$ MXene and induce a built-in electric field between n^+-Si and the $Ti_3C_2T_x$ MXene electrode to reduce the charge carrier recombination rate.

To gain more insight into the excellent solar cell performance of $Ti_3C_2T_x$ MXene contacted Si cells, optical characterizations were carried out. As shown in Figure 4c, n^+np^+-Si has low reflection and high absorption in the wavelength region of 400 to 1000 nm of the solar spectrum due to the pyramidal surfaces with SiN_x ARCs efficiently capturing the light and groove internal reflector surfaces with $Ti_3C_2T_x$ MXene contact allowing light to randomly bounce back into Si to improve absorption. It is known that the photoexcited charge carriers can easily be recombined on the surface defect sites that further leads to poor carrier collection efficiency. RTA was demonstrated to improve the contact parameters and reduce the leakage current and series resistivity. The external quantum efficiency (EQE) characterization for evaluating the photogenerated carrier generation and charge carrier collection efficiency of the solar cell was measured with $Ti_3C_2T_x$ MXene contacted Si cells before and after RTA (Figure 4d). The 300 °C annealed $Ti_3C_2T_x$ MXene/n^+np^+-Si exhibits an EQE of more than 90%, in the wavelength range from 450 to 900 nm, indicating that $Ti_3C_2T_x$ MXene can be used as a metal contact that effectively extracts photogenerated electrons from the Si solar cell and thereby improves the EQE in the wide wavelength range. Moreover, J_{sc} enhancement for the $Ti_3C_2T_x$ MXene/n^+np^+-Si solar cell after RTA treatment at 300 °C was calculated to be 37.2 mA cm^{-2} (Figure S9, Supporting Information) which is quite comparable with the observed current density value (36.7 mA cm^{-2}) from *J–V* characteristics (Figure 4a) of $Ti_3C_2T_x$ MXene/n^+np^+-Si solar cell. UV–vis transmittance curves of $Ti_3C_2T_x$ MXene films with different thickness are shown in Figure S10 in the Supporting Information. Similarly, UV–vis transmittance curves of drop casted thick $Ti_3C_2T_x$ MXene film before and after RTA treatment at 300 °C are depicted in Figure S11 in the Supporting Information. The transmittance curve for the MXene film before and after RTA treatment looks similar, indicating that the RTA process does not affect the transmittance of $Ti_3C_2T_x$ MXene films.

Delaminated few layered $Ti_3C_2T_x$ MXene contacted Si solar cell exhibits a maximum PCE of ≈11.5%. The Ohmic contact formation between metallic $Ti_3C_2T_x$ MXene and a heavily doped Si surface decreases contact resistance and suppresses charge carrier recombination, thus leading to excellent V_{oc} and J_{sc}. The RTA process improves electrical conductivity, reduces sheet resistance of $Ti_3C_2T_x$ MXene nanosheet films, and the cell series resistance of $Ti_3C_2T_x$ MXene contacted Si solar cells, leading to improved FF and overall PCE. This study demonstrates that solution processable MXene can be a potential contact material for optoelectronic devices.

Experimental Section

Synthesis of Ti_3AlC_2 MAX Phase: Ti_3AlC_2 MAX was synthesized based on the method of the previous report.[36] Commercially available Ti_2AlC powder and TiC powder were mixed together with a molar ratio of 1:1. Then, the powder mixture was ball milled for 24 h and then cold-pressed into a pellet. Afterward, the pellet was sintered at 1350 °C for 2.5 h under Ar atmosphere. Finally, the resulting pellet was crushed and sieved using 325 mesh, and then the Ti_3AlC_2 powder with a particle size of <44 µm was obtained.

Synthesis of Delaminated 2D $Ti_3C_2T_x$ MXene: Ti_3AlC_2 MAX (1 g) phase powder was immersed into a solution containing 9 M HCl (20 mL) and LiF (1 g). Then, the reaction mixture was stirred, and then cooled by an icebath to minimize localized heat from initial exothermic reaction.[36] The solution mixture was maintained at 35 °C using an oil bath for 24 h with continuous stirring. Afterward, the mixture was centrifuged and washed several times with excess deionized (DI) water. Each centrifugation cycle was performed at 3000 RCF for 5 min. The supernatant was discarded, and the sediment was collected and redispersed into DI water after hand shaking. The pH of the supernatant was achieved to ≈6 after several centrifugation cycles. The final centrifuge was performed at 500 RPM for 30 min after redispersing the collected $Ti_3C_2T_x$ MXene sediment in DI water. Finally, the supernatant colloidal solution containing delaminated 2D $Ti_3C_2T_x$ MXene flakes was collected and further used for the experiment.

Fabrication of $Ti_3C_2T_x$ MXene Drop-Casted n^+np^+-Si Solar Cells: Micropyramids and microgrooves were fabricated on opposite sides of 300 µm thick n-type (100) Si wafers (containing phosphorus as a dopant with 5×10^{15} cm^{-3} dopant concentration), separately. i) For the p^+-Si side, the textured micropyramids were fabricated by dipping as-cut Si substrates in the anisotropic etching solution consisting of KOH, isopropyl alcohol, and H_2O for 20 min.[50,53] A p^+ emitter layer (400 nm thick) was thermally diffused from the micropyramidal surface using a boron trichloride (BCl_3) source with a dopant concentration of 9×10^{19} cm^{-3} in a quartz tube furnace. Then, an Al_2O_3 surface passivation layer (7 nm) and an ARC of Si_3N_4 (70 nm) were deposited on top of the emitter layer (p^+ surface) using atomic layer deposition and plasma-enhanced chemical vapor deposition, respectively. Finally, an interdigitating Ag/Al electrode grid (300 nm) was deposited on the p^+-Si side of the device by inkjet-printing. ii) For the MXene/n^+-Si side, the microgrooves were fabricated by immersion in a mixture of KOH, water, and isopropyl alcohol to attain the randomly distributed microgroove surface textures.[50,54] The n^+ back surface field (BSF, 70 nm thick) was fabricated by the thermal diffusion of $POCl_4$ (dopant concentration of 3×10^{20} cm^{-3}) on the microgroove surface. Before depositing $Ti_3C_2T_x$ MXene, n^+-Si side was cleaned using HF to remove the oxide layer. Then, the prepared $Ti_3C_2T_x$ MXene colloidal solution was drop casted on the n^+-Si side and dried in the vacuum. Furthermore, the $Ti_3C_2T_x$ MXene drop-casted Si solar device was rapid thermal annealed at different temperatures from 100 to 400 °C for 30 s under Ar atmosphere by using the rapid thermal annealing processor.

Material and Electrical Characterizations: Field emission scanning electron microscope images were obtained with FEI Nova Nano 630. Raman spectra of the samples were collected from micro-Raman spectrometer (LabRAM ARAMIS, Horiba-Jobin Yvon). X-ray diffraction patterns were obtained from Bruker D2 phaser using Cu Kα radiation (λ = 1.5406 Å). Atomic force microscopy analysis was carried out using an Asylum Research (MFP-3D) scanning probe microscope in AC air mode. X-ray photoelectron spectroscopy analysis was performed using the Axis Ultra DLD system (Kratos, UK) equipped with Al Kα radiation source. The work function of $Ti_3C_2T_x$ MXene/n^+np^+-Si solar device was examined using scanning Kelvin probe microscopy equipped

with a commercial multifunction atomic force microscope (Cypher ES, Asylum Research Oxford Instruments) and Olympus (OMCL-AC240TM) Pt-coated cantilevers. The tip curvature radius was 15 nm, the quality factor was 190, and the resonance frequency used was 70 kHz. The surface roughness of $Ti_3C_2T_x$ MXene films were examined by NewView 7300 3D optical surface profiler using Zygo's coherence scanning interferometry technology. The contact angle measurement between $Ti_3C_2T_x$ MXene solution droplet and n^+-Si substrate was performed using a KRÜSS drop shape analyzer (DSA100). The UV–vis transmittance spectra of MXene film were obtained using UV–vis–NIR spectrophotometer (Shimadzu UV-3600). The electrical characterization of drop-casted $Ti_3C_2T_x$ MXene film before and after RTA process was acquired using Hall measurements (Sadhudesign, Source meter, SM6800 and VdP Probe, Model: NS6800).

Characterization of $Ti_3C_2T_x$ Drop-Casted n^+np^+-Si Solar Cell: Current–voltage (*I–V*) characteristics of $Ti_3C_2T_x$ MXene/n^+np^+-Si devices were measured in air using a Keithley 2400 precision source at AM1.5G (standard 1 sun) and 100 mW cm^{-2} illumination conditions. Prior to the *I–V* measurement, light illumination was calibrated to 1 sun intensity at room temperature using a 2×2 cm^2 Si calibration cell (Device code: RQN3724, ABET Inc.). The distance between solar light source and calibration cell (solar cells) was fixed to 15 cm. *I–V* measurement was performed from –0.1 to 0.6 V at a scan rate of 20 mV s^{-1}. The active area of the device was measured to be $\approx 1.1 \times 1.1$ cm^2 by using the photoshop software. The absorption, reflectance, and transmittance spectra were obtained for the wavelength region between 300 and 1100 nm using UV–vis–NIR spectrometer (Shimadzu UV-3600). The external quantum efficiency measurement was carried out for the wavelength ranging from 300 to 1100 nm using the spectral response system (Enli Technology Co., Ltd. R3011).

Supporting Information

Supporting Information is available from the Wiley Online Library or from the author.

Acknowledgements

H.C.F. and V.R. contributed equally to this work. Research reported in this publication was funded by King Abdullah University of Science and Technology (KAUST) Baseline Funds, KAUST Sensor Initiative, KAUST Solar Center, and KAUST Catalysis Center. X.S.F. acknowledges the support from the Science and Technology Commission of Shanghai Municipality (18520744600, 18520710800, and 17520742400).

Conflict of Interest

The authors declare no conflict of interest.

Keywords

2D materials, electrodes, metal contact, MXene, solar cells

Received: January 16, 2019
Revised: March 16, 2019
Published online:

[1] M. Zeng, Y. Xiao, J. Liu, K. Yang, L. Fu, *Chem. Rev.* **2018**, *118*, 6236.
[2] M.-L. Tsai, S.-H. Su, J.-K. Chang, D.-S. Tsai, C.-H. Chen, C.-I. Wu, L.-J. Li, L.-J. Chen, J.-H. He, *ACS Nano* **2014**, *8*, 8317.
[3] T. Roy, M. Tosun, J. S. Kang, A. B. Sachid, S. B. Desai, M. Hettick, C. C. Hu, A. Javey, *ACS Nano* **2014**, *8*, 6259.
[4] S. Lei, F. Wen, B. Li, Q. Wang, Y. Huang, Y. Gong, Y. He, P. Dong, J. Bellah, A. George, L. Ge, J. Lou, N. J. Halas, R. Vajtai, P. M. Ajayan, *Nano Lett.* **2015**, *15*, 259.
[5] C.-P. Lee, K.-Y. Lai, C.-A. Lin, C.-T. Li, K.-C. Ho, C.-I. Wu, S.-P. Lau, J.-H. He, *Nano Energy* **2017**, *36*, 260.
[6] Y.-H. Lin, S.-F. Lin, Y.-C. Chi, C.-L. Wu, C.-H. Cheng, W.-H. Tseng, J.-H. He, C.-I. Wu, C.-K. Lee, G.-R. Lin, *ACS Photonics* **2015**, *2*, 481.
[7] C.-H. Lin, B. Cheng, T.-Y. Li, J. R. D. Retamal, T.-C. Wei, H.-C. Fu, X. Fang, J.-H. He, *ACS Nano* **2019**, *13*, 1168.
[8] R. Vinoth, S. G. Babu, V. Bharti, V. Gupta, M. Navaneethan, S. V. Bhat, C. Muthamizhchelvan, P. C. Ramamurthy, C. Sharma, D. K. Aswal, Y. Hayakawa, B. Neppolian, *Sci. Rep.* **2017**, *7*, 43133.
[9] J. Jean, P. R. Brown, R. L. Jaffe, T. Buonassisi, V. Bulović, *Energy Environ. Sci.* **2015**, *8*, 1200.
[10] M. Bernardi, M. Palummo, J. C. Grossman, *Nano Lett.* **2013**, *13*, 3664.
[11] M. F. Bhopal, D. W. Lee, A. ur Rehman, S. H. Lee, *J. Mater. Chem. C* **2017**, *5*, 10701.
[12] D.-H. Lien, J. S. Kang, M. Amani, K. Chen, M. Tosun, H.-P. Wang, T. Roy, M. S. Eggleston, M. C. Wu, M. Dubey, S.-C. Lee, J.-H. He, A. Javey, *Nano Lett.* **2015**, *15*, 1356.
[13] X. Li, H. Zhu, K. Wang, A. Cao, J. Wei, C. Li, Y. Jia, Z. Li, X. Li, D. Wu, *Adv. Mater.* **2010**, *22*, 2743.
[14] Z. Zhang, T. Cui, R. Lv, H. Zhu, K. Wang, D. Wu, F. Kang, *J. Nanomater.* **2014**, *2014*, 1.
[15] X. Miao, S. Tongay, M. K. Petterson, K. Berke, A. G. Rinzler, B. R. Appleton, A. F. Hebard, *Nano Lett.* **2012**, *12*, 2745.
[16] X. Li, L. Fan, Z. Li, K. Wang, M. Zhong, J. Wei, D. Wu, H. Zhu, *Adv. Energy Mater.* **2012**, *2*, 425.
[17] T. Cui, R. Lv, Z.-H. Huang, S. Chen, Z. Zhang, X. Gan, Y. Jia, X. Li, K. Wang, D. Wu, F. Kang, *J. Mater. Chem. A* **2013**, *1*, 5736.
[18] X. Li, D. Xie, H. Park, M. Zhu, T. H. Zeng, K. Wang, J. Wei, D. Wu, J. Kong, H. Zhu, *Nanoscale* **2013**, *5*, 1945.
[19] M.-L. Tsai, M.-Y. Li, J. R. D. Retamal, K.-T. Lam, Y.-C. Lin, K. Suenaga, L.-J. Chen, G. Liang, L.-J. Li, J.-H. He, *Adv. Mater.* **2017**, *29*, 1701168.
[20] J. Ran, G. Gao, F.-T. Li, T.-Y. Ma, A. Du, S.-Z. Qiao, *Nat. Commun.* **2017**, *8*, 13907.
[21] M. Ghidiu, M. R. Lukatskaya, M.-Q. Zhao, Y. Gogotsi, M. W. Barsoum, *Nature* **2014**, *516*, 78.
[22] B. Anasori, M. R. Lukatskaya, Y. Gogotsi, *Nat. Rev. Mater.* **2017**, *2*, 16098.
[23] Z. W. Seh, K. D. Fredrickson, B. Anasori, J. Kibsgaard, A. L. Strickler, M. R. Lukatskaya, Y. Gogotsi, T. F. Jaramillo, A. Vojvodic, *ACS Energy Lett.* **2016**, *1*, 589.
[24] M. Naguib, M. Kurtoglu, V. Presser, J. Lu, J. Niu, M. Heon, L. Hultman, Y. Gogotsi, M. W. Barsoum, *Adv. Mater.* **2011**, *23*, 4248.
[25] L. Zhao, B. Dong, S. Li, L. Zhou, L. Lai, Z. Wang, S. Zhao, M. Han, K. Gao, M. Lu, X. Xie, B. Chen, Z. Liu, X. Wang, H. Zhang, H. Li, J. Liu, H. Zhang, X. Huang, W. Huang, *ACS Nano* **2017**, *11*, 5800.
[26] G. Gao, A. P. O'Mullane, A. Du, *ACS Catal.* **2017**, *7*, 494.
[27] R. B. Rakhi, B. Ahmed, M. N. Hedhili, D. H. Anjum, H. N. Alshareef, *Chem. Mater.* **2015**, *27*, 5314.
[28] X. Wu, Z. Wang, M. Yu, L. Xiu, J. Qiu, *Adv. Mater.* **2017**, *29*, 1607017.
[29] T. Y. Ma, J. L. Cao, M. Jaroniec, S. Z. Qiao, *Angew. Chem., Int. Ed.* **2016**, *55*, 1138.
[30] J. Pang, R. G. Mendes, A. Bachmatiuk, L. Zhao, H. Q. Ta, T. Gemming, H. Liu, Z. Liu, M. H. Rummeli, *Chem. Soc. Rev.* **2019**, *48*, 72.
[31] W. Bao, L. Liu, C. Wang, S. Choi, D. Wang, G. Wang, *Adv. Energy Mater.* **2018**, *8*, 1702485.
[32] M. R. Lukatskaya, S. Kota, Z. Lin, M.-Q. Zhao, N. Shpigel, M. D. Levi, J. Halim, P.-L. Taberna, M. W. Barsoum, P. Simon, Y. Gogotsi, *Nat. Energy* **2017**, *2*, 17105.

[33] C. J. Zhang, B. Anasori, A. Seral-Ascaso, S.-H. Park, N. McEvoy, A. Shmeliov, G. S. Duesberg, J. N. Coleman, Y. Gogotsi, V. Nicolosi, *Adv. Mater.* **2017**, *29*, 1702678.
[34] K. Hantanasirisakul, M.-Q. Zhao, P. Urbankowski, J. Halim, B. Anasori, S. Kota, C. E. Ren, M. W. Barsoum, Y. Gogotsi, *Adv. Electron. Mater.* **2016**, *2*, 1600050.
[35] Z. Kang, Y. Ma, X. Tan, M. Zhu, Z. Zheng, N. Liu, L. Li, Z. Zou, X. Jiang, T. Zhai, Y. Gao, *Adv. Electron. Mater.* **2017**, *3*, 1700165.
[36] Z. Wang, H. Kim, H. N. Alshareef, *Adv. Mater.* **2018**, *30*, 1706656.
[37] A. Lipatov, H. Lu, M. Alhabeb, B. Anasori, A. Gruverman, Y. Gogotsi, A. Sinitskii, *Sci. Adv.* **2018**, *4*, eaat0491.
[38] M. Sheoran, D. S. Kim, A. Rohatgi, H. F. W. Dekkers, G. Beaucarne, M. Young, S. Asher, *Appl. Phys. Lett.* **2008**, *92*, 172107.
[39] O. Balci, C. Kocabas, *Appl. Phys. Lett.* **2012**, *101*, 243105.
[40] J. Luo, W. Zhang, H. Yuan, C. Jin, L. Zhang, H. Huang, C. Liang, Y. Xia, J. Zhang, Y. Gan, X. Tao, *ACS Nano* **2017**, *11*, 2459.
[41] V. Presser, M. Naguib, L. Chaput, A. Togo, G. Hug, M. W. Barsoum, *J. Raman Spectrosc.* **2012**, *43*, 168.
[42] R. Liu, W. Li, *ACS Omega* **2018**, *3*, 2609.
[43] Z. Li, L. Wang, D. Sun, Y. Zhang, B. Liu, Q. Hu, A. Zhou, *Mater. Sci. Eng., B* **2015**, *191*, 33.
[44] M. Han, X. Yin, H. Wu, Z. Hou, C. Song, X. Li, L. Zhang, L. Cheng, *ACS Appl. Mater. Interfaces* **2016**, *8*, 21011.
[45] J. Halim, M. R. Lukatskaya, K. M. Cook, J. Lu, C. R. Smith, L.-Å. Näslund, S. J. May, L. Hultman, Y. Gogotsi, P. Eklund, M. W. Barsoum, *Chem. Mater.* **2014**, *26*, 2374.
[46] S. A. Shah, T. Habib, H. Gao, P. Gao, W. Sun, M. J. Green, M. Radovic, *Chem. Commun.* **2017**, *53*, 400.
[47] Y.-J. Yu, Y. Zhao, S. Ryu, L. E. Brus, K. S. Kim, P. Kim, *Nano Lett.* **2009**, *9*, 3430.
[48] C.-H. Lin, T.-Y. Li, B. Cheng, C. Liu, C.-W. Yang, J.-J. Ke, T.-C. Wei, L.-J. Li, A. Fratalocchi, J.-H. He, *Nano Energy* **2018**, *53*, 817.
[49] H.-P. Wang, J.-H. He, *Adv. Energy Mater.* **2017**, *7*, 1602385.
[50] H.-P. Wang, T.-Y. Lin, M.-L. Tsai, W.-C. Tu, M.-Y. Huang, C.-W. Liu, Y.-L. Chueh, J.-H. He, *ACS Nano* **2014**, *8*, 2959.
[51] L.-X. Wang, Z.-Q. Zhou, T.-N. Zhang, X. Chen, M. Lu, *Nanoscale Res. Lett.* **2016**, *11*, 453.
[52] S. R. Kodigala, in *Thin Films and Nanostructures*, Vol. *35* (Ed: K. Subba Ramaiah), Academic Press, New York **2010**, pp. 505–679.
[53] H.-P. Wang, T.-Y. Lin, C.-W. Hsu, M.-L. Tsai, C.-H. Huang, W.-R. Wei, M.-Y. Huang, Y.-J. Chien, P.-C. Yang, C.-W. Liu, L.-J. Chou, J.-H. He, *ACS Nano* **2013**, *7*, 9325.
[54] C.-A. Lin, K.-Y. Lai, W.-C. Lien, J.-H. He, *Nanoscale* **2012**, *4*, 6520.

